

# Self-Assembly and Characterization of Mesostructured Silica Films with a 3D Arrangement of Isolated Spherical Mesopores\*\*

By Kui Yu, Bernd Smarsly, and C. Jeffrey Brinker\*

We report the self-assembly and characterization of mesoporous silica thin films with a 3D ordered arrangement of isolated spherical pores. The preparation method was based on solvent-evaporation induced self-assembly (EISA), with MTES ( $\text{CH}_3\text{-Si}(\text{OCH}_2\text{CH}_3)_3$ ) as the silica precursor and a polystyrene-*block*-poly(ethylene oxide) (PS-*b*-PEO) diblock copolymer as the structure-directing agent. The synthetic approach was designed to suppress the siloxane condensation rate of the siloxane network, allowing co-self-assembly of the silica and the amphiphile, followed by retraction of the PEO chains from the silica matrix and matrix consolidation, to occur unimpeded. The calcined films retained the methyl ligands and exhibited no measurable microporosity, thereby indicating that the 3D-ordered spherical mesopores are not interconnected. A solvent-mediated formation mechanism is proposed for the absence of microporosity. Due to their closed porosity and hydrophobicity, the MTES-based films and MTES-TEOS ( $\text{Si}(\text{OCH}_2\text{CH}_3)_4$ )-based hybrid films we describe should be promising for applications such as low-*k* dielectrics.

## 1. Introduction

Silica films containing nanometer-scale mesopores with low dielectric constants ( $k < 2.2$ ), and good mechanical, chemical, and thermal stabilities, are desirable for future semiconductor devices.<sup>[1]</sup> In principle, there are two pathways to introduce nanoscale porosity into inorganic ceramic oxides. One is the use of a porogen, which yields a random arrangement of pores that become connected above the percolation threshold. Second are templating processes that take advantage of self-assembly and provide a relatively high degree of control in terms of the pore shape, pore size distribution, and structural regularity. Since the first preparation of mesostructured porous silica using a structure-directing surfactant was reported in 1992,<sup>[2]</sup> a great deal of interest in the synthesis of mesostructured porous inorganic oxides has developed.<sup>[3–5]</sup>

Here we attempt to formulate hydrophobic mesostructured porous silica thin films with isolated spherical voids. Our approach is based on so-called “solvent-evaporation-induced self-

assembly” (EISA),<sup>[3e,4d]</sup> with polystyrene-*block*-poly(ethylene oxide)(PS-*b*-PEO) as a structure-directing agent and MTES ( $\text{CH}_3\text{-Si}(\text{OCH}_2\text{CH}_3)_3$ ) as the silica precursor. The synthesis conditions were designed to minimize the siloxane condensation rate, thereby facilitating self-assembly. Pyrolysis was carefully performed to obtain mesostructured porous silica films, while retaining the methyl ligands. The films’ mesostructure was studied in detail by 2D grazing incidence small-angle X-ray scattering (GISAXS). Our results suggest that the films contain a closed-cell mesopore system with essentially no additional microporosity, due to removal of PEO from the inorganic matrix. The cause for the absence of microporosity is discussed, and a solvent-mediated formation mechanism is proposed. The present system is believed to be the first to form ordered mesostructured silica films using pure MTES as a silica precursor, and the first to result in an ordered arrangement of isolated pores.

## 2. Results and Discussion

Figure 1 shows representative transmission electron micrographs (TEMs) of the templated silica thin films (calcined (A–D) and uncalcined (E–F)). The films are usually crack-free, and have a thickness of 800–1000 nm. In the TEM images of the calcined samples, the bright circular regions are voids, which are very uniform in size and are arranged into highly ordered rectangular (B) or hexagonal (D) patterns, depending on the orientation. As estimated directly from these TEM micrographs, the average diameter of the mesopores is ca. 5–7 nm, while the average wall thickness is of the same order. These mesopore sizes obtained from TEM are the only accessible values, because neither sorption measurements nor GISAXS allowed the quantification of the mesopore size with sufficient accuracy. Before calcination, these bright spots are enriched with the diblock, namely the structure-directing agent; two

[\*] Dr. C. J. Brinker, Dr. K. Yu  
Sandia National Laboratories  
MS 1349, Albuquerque, NM 87185 (USA)  
E-mail: cjbrink@sandia.gov

Dr. C. J. Brinker, Dr. B. Smarsly  
Center for Micro-Engineered Materials, University of New Mexico  
Albuquerque, NM 87131 (USA)

[\*\*] This work was supported by Sandia National Laboratories, a Lockheed Martin Company, under Department of Energy Contract DE-AC04-94AL85000, the Air Force Office of Scientific Research Award Number F49620-01-1-0168, the DOE Office of Basic Energy Sciences, the DOD MURI Program Contract 318651, and Sandia’s Laboratory Directed Research and Development Program. Also, this work was supported by the ARL Collaborative Technology Alliance in Power and Energy, Cooperative Agreement No. DAAD19-01-2-0010. We thank Dr. Hongyon Fan and Mr. Nanguo Liu for help with the SAW measurements, Dr. Ralf Koehn for discussion on physisorption, and Dr. Roger A. Assink for the NMR measurements.

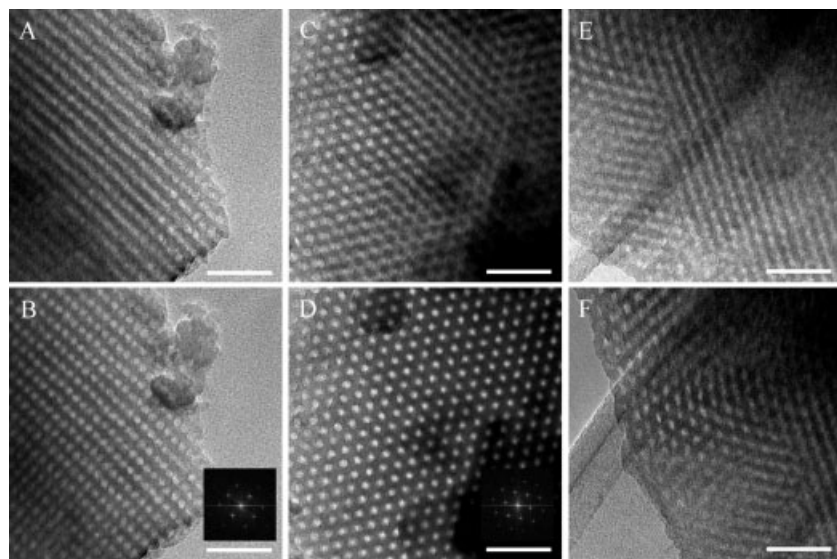


Fig. 1. TEM images of the mesostructured silica films prepared (A–D calcined, E–F as-cast). B and D are tilted ( $5^\circ$  in the  $x$  direction) from A and C, respectively. The scale bar is 50 nm. The insets in B and D are the Fourier transforms calculated from the whole area images.

TEM images of the uncalcined film are shown in Figures 1E and 1F, where the contrast between the silica matrix (darker regions with relatively high optical density) and the diblock spherical microdomains (lighter regions with increased brightness) is relatively small compared to that of the corresponding calcined sample shown in Figures 1A–D. Since the structures are comparable before and after calcination, the calcination step does not introduce a significant structural distortion.

From TEM it was difficult to distinguish unambiguously whether the bright circular features were attributable to cylindrical or spherical pores. The projected image of the spheres could overlap sufficiently to appear as either spheres or cylinders, depending on the orientation. Thus, tilting was performed to distinguish between spheres and cylinders. The fragments shown in Figures 1B and 1D were tilted ca.  $5^\circ$  about the  $x$ -axis from those shown in Figures 1A and 1C, respectively. It is evident in both sets of images that the mesopores are spherical rather than cylindrical. From Figures 1A and 1B it can be concluded that the spherical mesopores are placed on a rectangular lattice type, and the TEM images are best described by a cubic structure, which may be distorted in the direction normal to the substrate surface due to calcination. The fine structural details of these mesoporous films will be addressed in a detailed TEM study and are beyond the scope of this paper. While a face-centered cubic (fcc) lattice can not be fully excluded, based on a body-centered cubic (bcc) lattice, the orientations of the fragments shown in Figures 1B and 1D were determined as [011] and [111], respectively. The insets in Figures 1B and 1D are the Fourier transforms (in reciprocal space) calculated from the images. They confirm the cubic and hexagonal symmetries of the [011] and [111] orientations, respectively.

In addition to TEM, detailed GISAXS experiments were carried out to characterize both the meso- and microstructures of the same mesostructured porous silica films imaged in Figures 1A–D. Curve 1 (squares) in Figure 2A is the radially aver-

aged 2D GISAXS pattern of this calcined thin film. Below  $s=0.5 \text{ nm}^{-1}$  several Bragg reflections are present, which are consistent with the cubic symmetry of the mesoscale structure. The widths of the reflections and the slight deviation of the peak positions from an ideal cubic geometry also suggest a certain distortion of the cubic lattice. Similar to TEM, the GISAXS pattern suggests that the spherical mesopores are arranged in a bcc lattice. However, so far it is not possible to exclude an fcc structure. Under the assumption of a cubic bcc structure and a [011] orientation of the film relative to the substrate, the lattice parameter obtained from the GISAXS experiment was determined to be ca. 13 nm, which is in agreement with that directly measured from TEM micrographs (Fig. 1A–D). It is important to mention that the 2D GISAXS spot pattern itself (not shown) provides evidence for the orientation of the mesostructure with respect to the substrate.

In the large  $s$  region, a broad maximum is observed at  $s \approx 0.95 \text{ nm}^{-1}$ , indicating the presence of small units in the silica

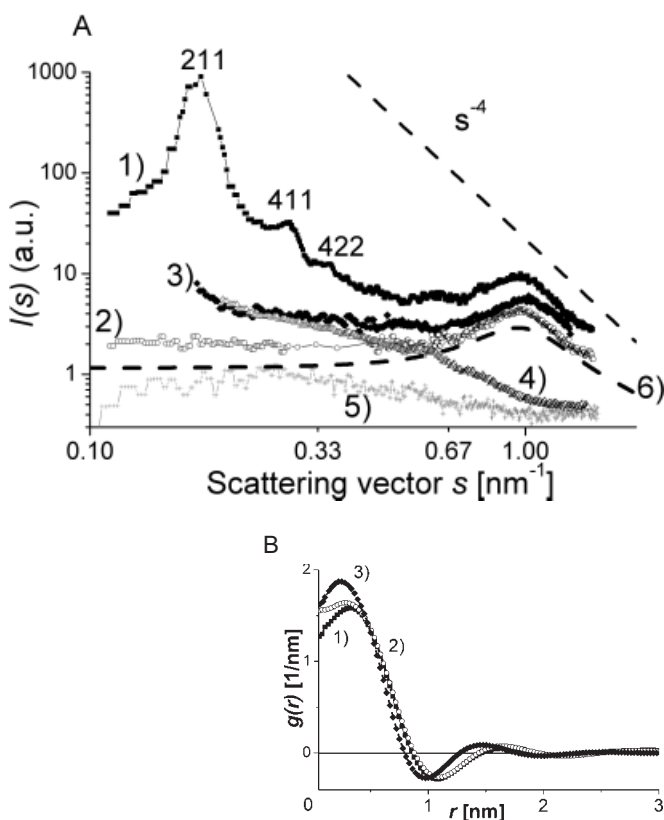


Fig. 2. A) SAXS curves 1–5. Curve 1 (squares) from the templated MTES-silica film, whose TEM images are shown in Figure 1A–D; curves 2 (circles) and 3 (diamonds) from the non-templated calcined and uncalcined MTES-silica films, respectively; curve 4 (triangles) from the calcined non-templated TEOS-silica film; and 5 (crosses) from the background; curve 6 is the simulated one. B) Chord-length distributions  $g(r)$ : curves 1 (squares), 2 (circles), and 3 (diamonds) are from curves 1 (squares), 2 (circles), and 3 (diamonds) in Figure 2A, respectively.

walls, separated from each other on the nanometer scale. In principle, contributions from any existing microporosity (caused by PEO removal), as well as from methyl ligands (in the silica matrix), should be apparent at large  $s$  in curve 1.<sup>[6]</sup> However, the SAXS intensity in this region could be a complex convolution of both contributions, so it is virtually impossible to distinguish between the contribution from micropores and methyl units based on curve 1 alone.

In order to resolve this uncertainty, reference GISAXS experiments were performed on silica films prepared without the PS-*b*-PEO template but calcined under the same conditions as the templated ones, using MTES or TEOS as the silica precursor. When TEOS was used, we denote the film as “TEOS-silica”, and when MTES was used, the film is denoted as “MTES-silica”. The curves 2 and 3 (circles and diamonds, respectively) in Figure 2A are the radially averaged GISAXS data from the non-templated MTES-silica films after and before calcination, respectively. Curve 4 (triangles) corresponds to a non-templated calcined TEOS-silica film and curve 5 (crosses) to the background (performed on a silicon wafer). These SAXS data were carefully acquired under almost identical experimental conditions, such as the same exposure time and angle of incidence. Therefore, we are able to compare semi-quantitatively the relative GISAXS intensities; due to the experimental procedure we were unable to obtain absolute intensities. It should be pointed out that curve 2 is shifted down slightly for better visualization, as curves 1, 2, and 3 overlap each other almost completely in the large  $s$  region.

First, for curves 2 and 4 (circles and triangles, respectively), at large  $s$  it is seen that the intensity of the calcined MTES-silica film (curve 2, circles) is approximately one order of magnitude higher than that of the calcined TEOS-silica film (curve 4, triangles), which in turn is similar to that of the background scattering (curve 5, crosses). Consequently, it is reasonable to conclude that it is the methyl ligand directly attached to Si that causes such a difference between curve 4 and 5. If there were a significant loss of the methyl ligands in the calcined MTES-silica film (curve 2), the shape and intensities of curves 2 and 3 should be significantly different. This result, namely the retention of CH<sub>3</sub> ligands, is consistent with our NMR data and a recent study on the thermal stability of MTES films.<sup>[7]</sup>

Second, since curves 2 (circles) and 3 (diamonds) are similar in both shape and intensity at large  $s$  with broad “maxima” at  $s \approx 0.95 \text{ nm}^{-1}$ , the microstructures of the corresponding non-templated calcined (curve 2) and non-templated uncalcined (curve 3) MTES-silica films are similar, implying that the number and distribution of CH<sub>3</sub> groups and any possible microporosity does not change significantly before and after calcination. Third, curves 1 and 2 are almost identical at large  $s$ , with broad “maxima” at  $s \approx 0.95 \text{ nm}^{-1}$ , and have comparable intensities. Thus, the microstructures for the templated and non-templated calcined MTES films are comparable. From the very similar shapes and relative intensities of the curves 1, 2 and 3 at large  $s$  and we can reasonably conclude that, a) methyl ligands give rise to the scattering in the large  $s$  region in curve 1, and b) no extra microporosity due to removal or calcination of PEO is present. It has to be pointed out that calcined MTES

films may be microporous (ca. 0.5–0.7 nm) after calcination at 400 °C in nitrogen, as was revealed by permeability measurements.<sup>[7]</sup> However, our GISAXS experiments indicate that the volume fraction of this intrinsic microporosity in the untemplated MTES films is significantly less than that of the methyl ligands. Although the volume fraction of the microporosity could not be quantified, it is estimated to be less than 4 % that of the uncalcined MTES film. While this kind of microporosity is certainly present in our materials, the GISAXS experiments show that there is almost no extra microporosity in the silica framework attributable to removal of the PEO chains.<sup>[6]</sup>

In conclusion, the scattering pattern at large scattering vectors in curves 1, 2, and 3 in Figure 2A results mainly from the distribution of methyl ligands in the silica matrix, and the broad “maxima” at  $s \approx 0.95 \text{ nm}^{-1}$  represent the average distances between CH<sub>3</sub> groups in these films.

In order to further check this interpretation, the GISAXS curve 3 of the uncalcined MTES film was simulated by a simple structural model, assuming a system of polydisperse spherical objects (CH<sub>3</sub> groups) distributed in a matrix. Our model for the spatial distribution is based on a modified hard-sphere potential (Percus–Yevick (PY) approach) with the average sphere diameter  $R_s$ , its variance  $\sigma_s$ , the PY radius  $R_{PY}$ , and the volume fraction  $\phi$  as fitting parameters.<sup>[6a]</sup> It is seen that a reasonable agreement is obtained between curve 2 and the fitted simulation curve 6 with  $\phi = 0.25 \pm 0.05$ ,  $R_{PY} = 0.43 \pm 0.04 \text{ nm}$ ,  $R_s = 0.2 \pm 0.05 \text{ nm}$ , and  $\sigma_s = 0.03 \pm 0.01 \text{ nm}$ , which is in conformity with the molecular size and the volume fraction of the CH<sub>3</sub> ligands. It is important to mention that the size variance,  $\sigma_s$ , obtained from the fit is quite small, as expected for the CH<sub>3</sub> groups. The finding that the GISAXS curve 6 can be described solely by this simple two-component structure model (CH<sub>3</sub>, SiO<sub>2</sub>) supports the interpretation that the GISAXS pattern of MTES-based films at large  $s$  is mainly determined by the Si–CH<sub>3</sub> groups, and that the intrinsic microporosity content (size ca. 0.4–0.6 nm<sup>[7]</sup>) is comparably small. The apparent similarity between curve 6 and curve 1 therefore indicates the absence of a significant additional SAXS contribution from micropores.

In addition to this simulation, a second method was employed to evaluate the GISAXS data.<sup>[6,8]</sup> The well-established concept of the “chord-length distribution” (CLD)<sup>[9]</sup> was recently applied to study microporosity in mesoporous silica powder materials templated by PS-*b*-PEO.<sup>[6]</sup> It was pointed out that the microporosity can be identified more reliably from this CLD approach, compared to traditional sorption techniques when porous materials consist of both meso- and micropores.<sup>[6,8]</sup> As shown in Figure 2A, a Porod-law asymptote ( $I(s) \propto s^{-4}$ ) is observed at large  $s$  in the SAXS curves 1, 2, and 3. Although the PY simulation presented above suggests that this  $s^{-4}$  asymptote may not be a true Porod law, but the tail of the quite broad maximum at  $s \approx 0.95 \text{ nm}^{-1}$ , the CLD method was applied, because it provides a characterization without assuming a specific structural model. The CLD curves 1 (squares), 2 (circles), and 3 (diamonds) in Figure 2B are obtained from curves 1 (squares), 2 (circles), and 3 (diamonds) in Figure 2A, respectively. These curves are almost identical on the  $r$  (nm) length-scale below 3.5 nm, indicating a close similarity of the microstructures, such as the average size, size distribution,

and average distance between the dispersed components.<sup>[9]</sup> For these curves, maxima are seen at ca. 0.4–0.5 nm, and minima at ca. 1 nm. Based on the theoretical concept of the chord-length distribution,<sup>[6,8,9]</sup> the maximum and the minimum represent the average size of the dispersed component in the matrix and average distance between the dispersed components, respectively. The CLD at small length scales and the value of  $g(0)$  reflect the topological properties of the interface such as curvature and angularity.<sup>[9]</sup> For an accurate determination of  $g(0)$ , a SAXS curve should cover scattering vectors up to  $s = 1.6 \text{ nm}^{-1}$ .<sup>[8]</sup>

It is commonly acknowledged that the size of a methyl ligand is ca. 0.4 nm, and the size of the micropores (produced by the removal of the PEO block in the mesoporous silica powder materials templated by PS-*b*-PEO) is ca. 0.8–2.0 nm.<sup>[6]</sup> Consequently, it is reasonable to attribute these small units to the methyl ligands rather than to PEO micropores. In addition, it is reasonable for the average distance between two methyl ligands to be ca. 0.8–0.9 nm, taking into account an average Si–O bond length of 0.16 nm. The values obtained from the CLD approach quantitatively indicate no significant change in the distribution upon calcination in argon. This analysis also suggests that it is the CH<sub>3</sub> unit that contributes to the scattering at large  $s$  in curve 1(squares) in Figure 2A.

The absence of microporosity is also in agreement with surface acoustic wave (SAW) measurements; the SAW thin film N<sub>2</sub> sorption technique is suitable for the characterization of pore sizes larger than 0.4 nm. Essentially no N<sub>2</sub> adsorption was detected for the calcined films shown in Figures 1A–D at relative pressures ( $P/P_0$ ) less than 0.8, indicating that the mesopores are isolated from each other and therefore not connected by micropores in the silica matrix.<sup>[11]</sup> An adsorption step at about  $P/P_0 = 0.8$  indicates the presence of the mesopores and hindered nitrogen sorption. It is generally acknowledged that the uptake beyond 0.8 ( $P/P_0$ ) may correspond to mesopore sizes larger than 10 nm.<sup>[12]</sup> For non-templated silica thin films prepared and calcined under the similar conditions, essentially no N<sub>2</sub> adsorption was detected by SAW measurements. Göltnner et al.<sup>[6c]</sup> reported that without any templates upon acid hydrolysis, silica precursors such as TEOS led to practically nonporous silica powder. A typical N<sub>2</sub> adsorption and desorption pattern (type IV) was observed for the calcined silica thin film, prepared with an ordered hexagonal arrangement of cylindrical mesopores using the same diblock copolymer template (but with a higher copolymer to silica precursor weight ratio).<sup>[5,11,12]</sup> Thus, a significantly different accessibility of the spherical and cylindrical pores is evident. Contact-angle measurements showed a high value of ca. 115° for the calcined film shown in Figures 1A–D, which is indicative of a relatively high hydrophobicity of the film, also confirming the presence of methyl ligands.<sup>[7]</sup> Thermal gravimetric analysis (TGA) of a PS-*b*-PEO diblock and a silica/PS-*b*-PEO hybrid film showed that the weight loss due to diblock decomposition was complete at ca. 400 °C in argon (Fig. 3). A small portion (ca. 1 %) of organic matter still seems to be present, which eventually may occupy micropores and lead to the inaccessibility of the mesopores. Since the thickness of the as-cast film is estimated to be less than 1 μm, we argue that the decomposition products

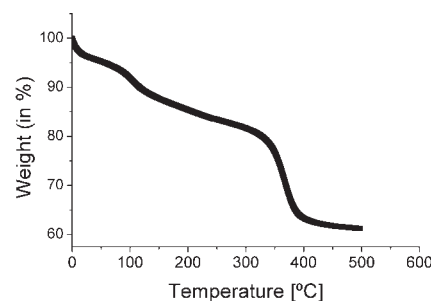


Fig. 3. TGA analysis for an as-prepared mesoporous silica film as shown in Figure 1. The heating rate was 5 °C min<sup>-1</sup> (argon atmosphere).

can diffuse through the silica matrix before it becomes impermeable to gas.<sup>[13]</sup> For the non-templated thin MTES films prepared under similar conditions, gas permeability (calcined at ca. 300 °C) and non-permeability (calcined at ca. 600 °C) were detected.<sup>[13]</sup> Consequently, the mesoporous films are best described by spherical voids, and only a small portion seem to be connected by micropores, which are 0.5 nm in size at most. In this sense, it seems justified to say that the spherical mesopores are closed cells without significant interconnection. To the best of our knowledge, there is little previous evidence of closed-cell mesoporous siliceous films. Nguyen et al. reported on closed-cell nanoporous poly(methylsilsequioxane) films; these, however, possess neither pores of uniform shape nor an ordered pore alignment.<sup>[14]</sup>

Solid-state <sup>29</sup>Si NMR measurements were performed to confirm the retention of Si–CH<sub>3</sub> groups after calcination. Figure 4

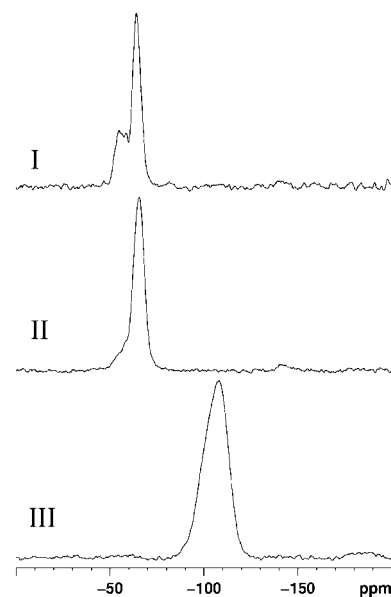


Fig. 4. <sup>29</sup>Si solid-state NMR spectra of scratched samples from a non-templated MTES-silica film: I) as-prepared, II) calcined in argon at 400 °C for 3 h, and III) calcined in air at 450 °C for 3 h.

shows <sup>29</sup>Si NMR spectra obtained from an as-prepared un-templated MTES film (I), the same film calcined at 400 °C in an argon atmosphere (II), and a film calcined at 450 °C in air (III). Both <sup>29</sup>Si spectra I and II consist of overlapped resonances in the range from –55 to –65 ppm, corresponding to trifunctional T-group silicons. The deconvolution into T<sup>2</sup> and T<sup>3</sup> components

(where 2 and 3 reflect the number of bridging oxygens surrounding the silicon center) shows that the  $T^3$  silicon resonance changes from  $-64.2$  (I) to  $-65.4$  ppm (II) and the extent of condensation of the siloxanes increases from 90.3 % (I) to 95.3 % (II). Thus, the elevated temperature treatment in an argon atmosphere has increased the extent of siloxane condensation, but the methyl groups remain intact. The change in chemical shift of  $T^3$  is related to an increase in strain upon calcination. Spectrum III comprises a single broad resonance in the range from  $-85$  to  $-120$  ppm, showing evidence of tetrafunctional Q, but no T silicons, thereby indicating complete oxidation of the Si-CH<sub>3</sub> bonds in air at 450 °C. Deconvolution into Q<sup>2</sup>, Q<sup>3</sup>, and Q<sup>4</sup> resonances provides an estimate of reaction of 92.6 %, slightly lower than that of the T silicons. The lower extent of reaction of the Q-group silicons compared to that of the T-group silicons reflects a higher reactivity of the T silicons.

To explain the absence of microporosity expected from PEO removal for the templated calcined silica films, a solvent-mediated model for the PS-*b*-PEO diblock templating mechanism is suggested. For block copolymer templates with PEO as the hydrophilic block, it is generally assumed that in the process of self-assembly the PEO chains interact through hydrogen bonding with the hydrophilic inorganic silicic acid, thereby serving to establish the wall thickness.<sup>[1]</sup> In the case of the films studied here, it is tempting to speculate that in the early stage of solvent evaporation, the PEO is well-solvated by the hydrophilic polysilicic acid matrix, but retracts from the matrix at a later stage of drying or consolidation.

It is generally acknowledged that the radius of gyration  $R_g$  of a polymeric coil in solution is

$$R_g^2 = \frac{b^2 N^{2\nu}}{6} \quad (1)$$

where  $b$  is the statistical segment length,  $N$  is the number of segments, and  $\nu$  is the Flory exponent, which depends on whether the block is in a good, theta, or bad solvent, as defined by the respective Flory  $\chi$  parameter:

$$\nu = \begin{cases} 3/5 & \chi < 1/2 & \text{Good} \\ 1/2 & \chi \approx 1/2 & \text{Theta} \\ 1/3 & \chi > 1/2 & \text{Bad} \end{cases} \quad (2)$$

During the initial stage of evaporation, the solvent composition changes from principally tetrahydrofuran (THF), a good solvent for PS, to water/silicic acid, a theta solvent for PS. Correspondingly, the  $R_g$  of the PEO block is expected to decrease. Subsequently, in the later stage of solvent evaporation, the interaction between the PEO and the polysilicic acid is expected to decrease due to the depletion of water needed to mediate such interactions through hydrogen bonding and due to the onset of siloxane condensation that consumes hydrophilic silanols. The combined effect of the changing solvent composition and the changing solvation properties of the silicic acid framework are illustrated schematically in Figure 5. Starting from an arbitrary state in which both blocks are well solvated (Fig. 5A), evaporation of THF enriches the system in water and silicic acid causing shrinkage of the PS block, which exerts a radially

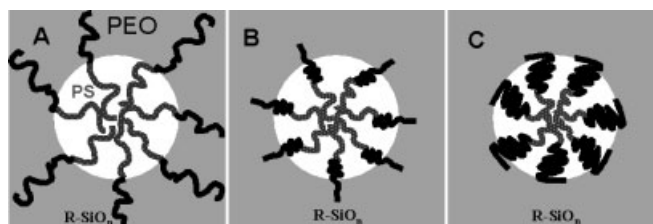


Fig. 5. Schematic illustration of the proposed solvent-mediated mechanism to form silica/PS-*b*-PEO hybrid materials via EISA with isolated pores. The black and gray lines represent the PS and PEO blocks, respectively: A) “2-phase” structure, namely the PEO/inorganic matrix and the PS; B) transition from (A) to (C); C) “3-phase” structure, namely the inorganic matrix, the PEO, and the PS. During EISA, evaporation and the incipient stages of siloxane condensation cause a progressive reduction in solvent quality and correspondingly a change from (A) to (B) to (C). The silica matrix continually rearranges to avoid the formation of micropores.

oriented tensile stress on the PEO block and initiates its retraction from the silicate matrix. Ensuing evaporation of water reduces hydrogen-bonding interactions and increases the PEO concentration promoting further PEO phase separation. Because the silica matrix is weakly condensed it can rearrange to accommodate the lost PEO without the need to induce of microporosity (Fig. 5B), as is generally observed for mesoporous powders templated by PS-*b*-PEO.<sup>[6]</sup> This phase separation process continues until the PEO block retracts almost completely, forming a thicker layer at the interface between the PS microdomains and the silica, a “3-phase” structure composed of the inorganic silica, the PEO, and the PS, as shown in Figure 5C. Because the PEO retraction is accompanied by rearrangement and consolidation of the silica matrix, no microporosity is induced. The schemes depicted in Figures 5A and 5B have been used to rationalize the formation of other block-copolymer-templated silica.<sup>[6,15]</sup> In some of these cases it is likely that intervening siloxane condensation freezes in the corresponding structure so that PEO removal creates microporosity interconnecting the mesopores.<sup>[6]</sup>

### 3. Conclusions

Through evaporation-induced self-assembly (EISA), mesostructured silica films with spherical mesopores organized in an oriented 3D array were synthesized using MTES (Si(OCH<sub>2</sub>CH<sub>3</sub>)<sub>3</sub>CH<sub>3</sub>) as the silica precursor and PS-*b*-PEO as the surfactant. TEM and GISAXS measurements showed the films to consist of isolated spherical voids with almost no interconnecting microporosity due to loss of PEO. We propose a solvent-mediated formation mechanism and advocate that suppression of siloxane condensation allowed phase separation/retraction of the PEO from the silica matrix to occur without inducing microporosity. GISAXS and NMR studies show that the methyl groups are randomly dispersed in the silica matrix and retained after calcination. Concerning the utilization of porous materials as low- $k$  dielectric insulators, cubic arrangements of isolated spherical pores are expected to maximize the modulus (for a given porosity) and minimize interdiffusion of metals. Retention of CH<sub>3</sub> moieties should reduce the

framework dielectric constant and impart hydrophobicity. Thus the PS-*b*-PEO templated films we describe and related ordered closed-porosity films should be of general interest to the microelectronics community.

## 4. Experimental

In a typical synthesis, PS(35)-*b*-PEO(109) diblock copolymer, which has 35 styrene units and 109 ethylene oxide units, was dissolved in tetrahydrofuran (THF) at 1 wt.-%. PS(35)-*b*-PEO(109) was purchased from Polymer Source, Inc. Afterwards, a certain amount of methyl triethoxysilane (MTES, CH<sub>3</sub>-Si(OCH<sub>2</sub>CH<sub>3</sub>)<sub>3</sub>), hydrogen chloride (HCl), and water (MilliQ) were added to the dilute copolymer solution in THF. The quantity of MTES added was such as to achieve a weight ratio of ca. 1:7 copolymer/precursor. The total amount of HCl and water added was such so as to achieve molar ratios of 1:0.004:5 MTES/HCl/H<sub>2</sub>O. After 30 min of sonication, one drop of the solution was cast on a silicon wafer to obtain a silica/diblock thin film. Calcination in argon (with a heating rate of 1°C min<sup>-1</sup> to 400°C for 3 h) removed the diblock and produced mesostructured porous silica films. A detailed description can be found elsewhere [5]. It was attempted to determine the film thickness by spectral ellipsometry, but no usable data was obtained, probably because the films do not show a uniform thickness. Based on a simple calculation regarding the area covered by the films and the mass, the thickness of the films was approximately 800–1000 nm.

The meso- and microstructures were characterized by transmission electron microscopy (TEM) and grazing incidence small-angle X-ray scattering (GISAXS). The TEM study was performed using a JEOL 2010 TEM at an acceleration voltage of 200 kV; the samples were prepared by scratching the films with tweezers and directly dispersing the film fragments onto carbon copper grids. The GISAXS measurements were performed directly on cast thin films, using the 5 m pinhole instrument (Rotaflex, Rigaku) in the SAXS laboratory at the Center for Micro-Engineered Materials at the University of New Mexico, with an available range of scattering vectors between  $s = 0.08\text{--}1.4\text{ nm}^{-1}$ , where  $s = 2 \sin(\theta)/\lambda$  ( $q = 2s$ ),  $2\theta$  is the scattering angle, and  $\lambda$  the Cu K $\alpha$  wavelength (0.154 nm). The GISAXS experimental setup (such as the distance between the detector and the sample) was designed to investigate both meso- and microstructures of the thin films at the same time. A surface acoustic wave (SAW) nitrogen sorption technique was used to determine pore accessibility of our calcined films; a detailed description of the SAW measurement can be found elsewhere [3e]. Thermal Gravimetric Analysis (TGA) was performed using a Thermal Sciences STA 1500 instrument with a heating rate of 1°C min<sup>-1</sup> to 600°C. Contact angle measurements were performed on a VCA 2000 (Video Contact Angle System) instrument to qualitatively monitor hydrophobicity of the prepared thin films. Magic angle spinning (MAS) solid-state nuclear magnetic resonance (NMR) spectroscopy experiments were carried out on a Bruker AMX spectrometer. The <sup>29</sup>Si NMR experiments were performed at 79.5 MHz using direct polarization and high-powered 1H decoupling, with a delay time of 240 sec and 64 scans; the

samples were spun at 6 kHz in a 7 mm MAS probe. A range of delay times was used for each of the samples in order to provide quantitative results for both the <sup>29</sup>Si NMR experiments.

Received: August 12, 2002

- [1] R. D. Miller, *Science* **1999**, *286*, 421.
- [2] C. Kresge, M. Leonowicz, W. Roth, C. Vartuli, J. Beck, *Nature* **1992**, *359*, 710.
- [3] a) M. Ogawa, *J. Am. Chem. Soc.* **1994**, *116*, 7941. b) Q. Huo, D. I. Margolese, U. Clesla, P. Feng, T. E. Gler, P. Slegler, R. Leon, P. M. Petroff, F. Schuth, G. D. Stucky, *Nature* **1994**, *368*, 317. c) P. T. Tanev, T. J. Pinnavaia, *Science* **1995**, *267*, 865. d) T. Markus, A. Franck, A. D. Chesne, H. Leist, Y. Zhang, R. Ulrich, V. Schadler, U. Wiesner, *Science* **1997**, *278*, 1795. e) Y. Lu, R. Ganguli, C. Drewien, M. Anderson, C. Brinker, W. Gong, Y. Guo, H. Soyez, B. Dunn, M. Huang, J. Zink, *Nature* **1997**, *389*, 364. f) Q. Huo, D. I. Margolese, G. D. Stucky, *Chem. Mater.* **1996**, *8*, 1147.
- [4] a) D. M. Antonelli, J. Y. Ying, *Angew. Chem. Int. Ed. Engl.* **1995**, *34*, 2014. b) S. Mann, G. A. Ozin, *Nature* **1996**, *382*, 313. c) G. A. Ozin, E. Chomski, D. Khushalani, M. J. MacLachlan, *Curr. Opin. Colloid Interface Sci.* **1998**, *3*, 181. d) C. J. Brinker, Y. Lu, A. Sellinger, H. Fan, *Adv. Mater.* **1999**, *11*, 579.
- [5] a) K. Yu, C. J. Brinker, A. J. Hurd, A. Eisenberg, *Polym. Prepr. (Am. Chem. Soc., Div. Polym. Chem.)* **2001**, *42*, 659. b) K. Yu, C. J. Brinker, A. J. Hurd, A. Eisenberg, *Polym. Mater. Sci. Eng. Prepr.* **2001**, *84*, 796. c) K. Yu, C. A. Drewien, C. J. Brinker, A. J. Hurd, A. Eisenberg, *Mater. Res. Soc. Symp. Proc.* **2001**, *672*, O8.15. d) K. Yu, A. J. Hurd, C. J. Brinker, A. Eisenberg, *Langmuir* **2001**, *17*, 7961. e) K. Yu, B. Smarsly, C. J. Brinker, *Mater. Res. Soc. Symp. Proc.* **2002**, *728*, S1.9.
- [6] a) B. Smarsly, C. Göltner, M. Antonietti, W. Ruland, E. Hoinkis, *J. Phys. Chem. B* **2001**, *105*, 831. b) B. Smarsly, S. Polarz, M. Antonietti, *J. Phys. Chem. B* **2001**, *105*, 10473. c) C. G. Göltner, B. Smarsly, B. Berton, M. Antonietti, *Chem. Mater.* **2001**, *13*, 1617.
- [7] a) R. M. de Vos, W. F. Maier, H. Verweij, *J. Membr. Sci.* **1999**, *158*, 277. b) R. M. de Vos, *High-Selectivity, High-flux Silica Membranes for Gas Separation*, Ph.D. Thesis, Printpartners, Ipskamp, Enschede **1998**.
- [8] B. Smarsly, M. Antonietti, T. Wolff, *J. Chem. Phys.* **2002**, *116*, 2618.
- [9] a) J. Méring, D. Tchoubar, *J. Appl. Crystallogr.* **1968**, *1*, 153. b) R. Perret, W. Ruland, *J. Appl. Crystallogr.* **1970**, *3*, 525. c) S. Torquato, B. Lu, *Phys. Rev. E* **1993**, *47*, 2950.
- [10] C. A. Fyfe, P. P. Aroca, *J. Phys. Chem. B* **1997**, *101*, 9504.
- [11] K. Yu, H. Fan, C. J. Brinker, unpublished.
- [12] K. S. W. Sing, D. H. Everett, R. A. W. Haul, L. Moscou, R. A. Pierotti, J. Rouquerol, T. Siemieniowska, *Pure Appl. Chem.* **1985**, *57*, 603.
- [13] a) K. Yu, G. Xomeritakis, C. J. Brinker, unpublished. b) N. K. Raman, C. J. Brinker, *J. Membr. Sci.* **1995**, *105*, 273.
- [14] C. V. Nguyen, K. R. Carter, C. J. Hawker, J. L. Hedrick, R. L. Jaffe, R. D. Miller, J. F. Remenar, H.-W. Rhee, P. M. Rice, M. F. Toney, M. Trollsas, D. Y. Yoon, *Chem. Mater.* **1999**, *11*, 3080.
- [15] S. M. D. Paul, J. W. Zwanziger, R. Ulrich, U. Wiesner, H. W. Spiess, *J. Am. Chem. Soc.* **1999**, *121*, 5727.